GRAIL Gravity Field Determination Using the Celestial Mechanics Approach

Daniel Arnold[a,], Stefano Bertone[a], Adrian Jäggi[a], Gerhard Beutler[a], Leos Mervart[b]

[a] *Astronomical Institute of the University of Bern, Sidlerstrasse 5, 3012 Bern, Switzerland*
[b] *Institute of Advanced Geodesy, Czech Technical University, Thakurova 7, 16629 Prague 6-Dejvice, Czech Republic*

Abstract

The NASA mission GRAIL (Gravity Recovery and Interior Laboratory) inherited its concept from the GRACE (Gravity Recovery and Climate Experiment) mission to determine the gravity field of the Moon.

We present lunar gravity fields based on the data of GRAIL's primary mission phase. Gravity field recovery is realized in the framework of the Celestial Mechanics Approach, using a development version of the Bernese GNSS Software along with Ka-band range-rate data series as observations and the GNI1B positions provided by NASA JPL as pseudo-observations.

By comparing our results with the official level-2 GRAIL gravity field models we show that the lunar gravity field can be recovered with a high quality by adapting the Celestial Mechanics Approach, even when using pre-GRAIL gravity field models as a priori fields and when replacing sophisticated models of non-gravitational accelerations by appropriately spaced pseudo-stochastic pulses (i. e., instantaneous velocity changes).

We present and evaluate two lunar gravity field solutions up to degree and order 200 — AIUB-GRL200A and AIUB-GRL200B. While the first solution uses no gravity field information beyond degree 200, the second is obtained by using the official GRAIL field GRGM900C up to degree and order 660 as a priori information. This reduces the omission errors and demonstrates the potential quality of our solution if we resolved the gravity field to higher degree.

Keywords:
Moon, Gravity, Orbit determination, Celestial Mechanics, Moon, interior

1. Introduction

The NASA mission Gravity Recovery and Interior Laboratory (GRAIL) is the latest and most sophisticated satellite mission for the determination of the lunar gravity field (Zuber et al., 2013b). It consists of two satellites, GRAIL-A ("Ebb") and GRAIL-B ("Flow"), launched on 10 September 2011, and entering nearly polar lunar orbits in the beginning of 2012. Data for gravity field recovery was acquired during two science phases, given by the requirement that the elevation of the Sun above the orbital plane is large enough for the solar panels to produce enough power. In the primary mission (PM) phase (1 March to 29 May 2012) the mean altitude of the two satellites was 55 km above the lunar surface (corresponding to a revolution period of about 113 minutes). The eccentricity of the orbits varied between around 0.02 at the beginning and end of the PM phase and 0.003 in the middle, while the inclination changed between 89.9° and 88.5° with a bimonthly period. In the extended mission (EM) phase (30 August to 14 December 2012) the orbits were lowered to 23 km on average (Zuber et al., 2013a). The separation between the two spacecraft varied from 40 km to 220 km during the mission to find a compromise between sensitivity and multipath effects on the inter-satellite communications (Konopliv et al., 2013). The mission ended with a controlled crash of the two probes on the Moon on 17 December 2012.

Email address: daniel.arnold@aiub.unibe.ch (Daniel Arnold)

The concept of the mission was inherited from the Earth-orbiting mission Gravity Recovery and Climate Experiment (GRACE, Tapley et al., 2004) in that the key observations consisted of ultra-precise inter-satellite Ka-band range measurements (Asmar et al., 2013). The use of these observations enables data acquisition even when the spacecraft are not Doppler-tracked from the Earth. Together with the one- and two-way Doppler observations from the NASA Deep Space Network (DSN), GRAIL data allows for a determination of the lunar gravity field with an unprecedented accuracy for both the near- and the far-side of the Moon. Its results are essential to improve the understanding of the Moon's internal structure and thermal evolution (Wieczorek et al., 2013).

The official GRAIL gravity field models based on PM data consist of spherical harmonic (SH) coefficients up to degree and order 660 [GL0660B (Konopliv et al., 2013) and GRGM660PRIM (Lemoine et al., 2013)], while the latest models resolve the selenopotential up to degree and order 900 [GL0900D (Konopliv et al., 2014) and GRGM900C (Lemoine et al., 2014)] by using both PM and EM data. These solutions were obtained using the software packages MIRAGE, a gravity processing version of the JPL Orbit Determination Program (ODP, Moyer, 2003), and GEODYN (Pavlis et al., 2013), respectively.

Apart from the Ka-band range and Doppler data, satellite positions (GNI1B positions) of the GRAIL probes from the dynamic orbit determination performed at JPL are also available. As explained by Jäggi et al. (2015), the usage of these positions as pseudo-observations allows for a relatively straightforward adaption of our gravity field recovery procedures from GRACE (Jäggi et al., 2008), where GPS-derived kinematic positions are available, to GRAIL without having first to implement Doppler data processing. These adaptions are performed within a development version of the Bernese GNSS Software (Dach et al., 2007). The use of GNI1B positions is only considered an intermediate solution for our approach as it will not lead to a completely independent gravity field solution.

In addition to normalized spherical harmonic coefficients up to degree 200, we set up arc- and satellite-specific parameters (like initial state vectors and pseudo-stochastic pulses) as common parameters for all measurement types (see Sec. 2 for more details). Pseudo-stochastic pulses shall compensate for imperfect models of non-gravitational accelerations, e. g., caused by solar radiation pressure.

This paper is structured as follows. In Sec. 2 we briefly review the Celestial Mechanics Approach (CMA) for gravity field determination. Section 3 discusses some results for the initial orbit determination of the GRAIL satellites and outlines the performance of our data modeling, paying attention to possible limitations due to missing radiation pressure modeling. We point out that up to release 2 of the level-1b data the estimation of a Ka-band time bias is mandatory (see Sec. 3.3). In Sec. 4 we focus on gravity fields obtained by using the CMA. We present our lunar gravity field solutions up to degree and order 200. Section 5 gives an outlook on possible further improvements to our orbit and gravity field modeling. Section 6 presents our final remarks and conclusions.

2. The Celestial Mechanics Approach

The Celestial Mechanics Approach (CMA, Beutler et al., 2010) treats gravity field recovery as an extended orbit determination problem. It is a dynamic approach allowing for pseudo-stochastic parameters to absorb force model deficiencies.

For a GRAIL probe the equations of motion in the inertial system read as

$$\ddot{\vec{r}} = -GM_M \frac{\vec{r}}{r^3} + \vec{f}(t, \vec{r}, \dot{\vec{r}}, q_1, ..., q_d) \; , \tag{1}$$

where GM_M denotes the gravity parameter of the Moon, $\vec{r}$ is the selenocentric position of the probe and $\vec{f}$ collects all perturbing accelerations as described in Sec. 2.1. Dots indicate derivatives w. r. t. time. The second-order differential equations (1) require six initial or boundary conditions for a particular solution. In the framework of the CMA satellite motion is described as an initial value problem [1]. The initial conditions $\vec{r}(t_0) = \vec{r}(a, e, i, \Omega, \omega, u; t_0)$ and $\dot{\vec{r}}(t_0) = \dot{\vec{r}}(a, e, i, \Omega, \omega, u; t_0)$ at an initial epoch t_0 are defined by six Keplerian

[1] See Klinger et al. (2014) for a boundary value approach to GRAIL gravity field recovery.

osculating elements. a denotes the semi-major axis, e the numerical eccentricity, i the inclination w. r. t. the equatorial plane, Ω the right ascension of the ascending node, ω the argument of periapsis, and u the argument of latitude at time t_0. $q_1, ..., q_d$ parametrize the perturbing accelerations and are both arc-specific orbit parameters (e. g., empirical accelerations) and general parameters such as gravity field coefficients. Let us denote the $6 + d$ parameters (initial conditions and q_i) collectively as p_i.

2.1. Perturbing accelerations

The perturbing accelerations $\vec{f}$ on the right-hand side of the equations of motion (1) are given by

$$\vec{f} = T_f^i \nabla V + \vec{a}_b + \vec{a}_t + \vec{a}_r + \vec{a}_n + \vec{a}_e \ , \tag{2}$$

where V denotes the lunar gravity potential in the Moon-centered body-fixed reference frame, T_f^i is a rotation matrix relating the Moon-centered body-fixed with the inertial system, $\vec{a}_b$ are the third-body accelerations, $\vec{a}_t$ denote accelerations due to the tidal deformation of the Moon, $\vec{a}_r$ are relativistic corrections, $\vec{a}_n$ non-gravitational accelerations and $\vec{a}_e$ empirical accelerations.

2.1.1. The gravity potential

The gravitational acceleration $\vec{a}_g \doteq T_f^i \nabla V$ exerted by the Moon is written in terms of the lunar gravity potential V, which is expressed using a standard spherical harmonics (SH) expansion (Heiskanen and Moritz, 1967) as

$$V(r, \lambda, \phi) = \frac{GM_M}{r} \sum_{l=1}^{l_{max}} \left(\frac{R_M}{r} \right)^l \sum_{m=0}^{l} \bar{P}_{lm}(\sin\phi) \cdot \left[\bar{C}_{lm} \cos(m\lambda) + \bar{S}_{lm} \sin(m\lambda) \right] \ , \tag{3}$$

where R_M is the reference radius (1738 km) of the Moon and r, λ and ϕ denote the selenocentric radius, longitude and latitude of the evaluation point, respectively. $\bar{P}_{lm}$ are the fully normalized associated Legendre functions of degree l and order m, and $\bar{C}_{lm}$ and $\bar{S}_{lm}$ are the corresponding SH coefficients. For the lunar body-fixed reference system, we use the Principal Axes (PA) system with axes coinciding with the principal axes of inertia of the Moon. The Euler (libration) angles connecting the International Celestial Reference System (ICRS)[2] with the PA system are taken from the DE421 JPL ephemerides (Folkner et al., 2009).

In this article we present lunar gravity field solutions up to a maximum degree $l_{max} = 200$.

2.1.2. Third-body accelerations

We take third-body accelerations due to Earth, Sun, Jupiter, Venus and Mars into account. These celestial bodies are all approximated as point masses with positions taken from the JPL ephemerides DE421.

2.1.3. Tidal acceleration

The tidal deformation of the Moon due to other celestial bodies causes an additional acceleration acting on the GRAIL probes. According to the IERS2010 conventions (Petit and Luzum, 2010) this acceleration can be expressed in terms of a change of the (tide-free) SH gravity field coefficients as

$$\Delta\bar{C}_{lm} - i\Delta\bar{S}_{lm} = \frac{k_{lm}}{2l+1} \sum_{j=2}^{3} \frac{GM_j}{GM_M} \left(\frac{R_M}{r_j} \right)^{l+1} \cdot \bar{P}_{lm}(\sin\Phi_j) e^{-im\lambda_j} \ , \tag{4}$$

where j labels the perturbing body (Earth and Sun) of mass M_j. r_j, λ_j and Φ_j denote the spherical coordinates of the perturbing body in the lunar body-fixed system and the constants k_{lm} are the Love numbers. We consider only identical forcing and response degrees and orders (2,0), (2,1), (2,2) and (3,0).[3] The values for the corresponding Love numbers are taken from Lemoine et al. (2013) and not improved during gravity field determination.

[2] Aligned with the mean equator and dynamical equinox of J2000.0.

[3] See eq. (6.6) of Petit and Luzum (2010).

2.1.4. Non-gravitational accelerations

The most important non-gravitational acceleration is caused by direct and indirect solar radiation pressure. Furthermore, thermal radiation of the satellite body induces a further acceleration, about 5 times smaller than the acceleration due to direct solar radiation pressure (Fahnestock et al., 2012). Currently, we do not model any of these non-gravitational accelerations but absorb them with empirical accelerations (see Sec. 2.1.5) and pseudo-stochastic pulses (see Sec. 2.1.6).

2.1.5. Empirical accelerations

Empirical accelerations can be set up in pre-defined directions (radial, along-track and cross-track) as constant or as periodic terms with given periods. The constants and the coefficients of the periodic terms are estimated in the least-squares adjustment. Empirical accelerations are an efficient way to absorb unmodeled forces (Jäggi et al., 2006).

2.1.6. Pseudo-stochastic pulses

Pseudo-stochastic pulses are instantaneous velocity changes in pre-defined directions (radial, along-track and cross-track) at user-defined epochs, which can be estimated in the least-squares adjustment (Beutler et al., 2010). They allow for an efficient absorption of non-gravitational perturbations. While pseudo-stochastic pulses are non-physical — they do not appear on the right hand side of the equations of motion (1) — they are in principle a means to generate different contiguous short-arc solutions (the generation of usual, non-contiguous short-arcs would require the estimation of additional offsets at the specified times).

2.2. Gravity field recovery

2.2.1. Initial orbit determination

In a first step, a priori orbits $\vec{r}_0(t)$ are derived on a daily basis from GNI1B positions (Kahan, 2014). Based on a fixed background gravity field the equations of motion (1) are numerically integrated. In addition, the partial derivatives of the orbit w. r. t. the parameters are obtained by numerically integrating the variational equations, as outlined in Beutler (2005). This allows in a second step for a single least-squares adjustment of arc-specific parameters to fit both the GNI1B positions and the Ka-band observations. Apart from the initial Keplerian osculating elements the following arc-specific empirical parameters are set up:

- Once-per-revolution unconstrained empirical accelerations in the radial (R), along-track (S) and cross-track (W) directions over the entire arc-length of 1 day;
- Pseudo-stochastic pulses in R/S/W-directions and constrained to zero with an a priori standard deviation of 0.1 m/s (which is basically free but used to avoid singularities). The spacing of the pulses was set between 10 min and 40 min (see Sec. 4.1).

For some of the solutions presented here, an additional constant empirical acceleration in radial direction is estimated, since we do not solve for the degree 0 of the selenopotential (GM_M). Differently from other approaches, no scaling factors to a priori background models nor instrument-specific parameters are set up to absorb deficiencies in the force modeling.

2.2.2. Generalized orbit determination

The actual gravity field recovery is set up as a generalized orbit improvement of the previously computed a priori orbits $\vec{r}_{0j}(t)$ ($j = 1, 2$ labels the satellites), which are represented by a set of a priori parameter values p_{0ij}, with $i = 1, \ldots, 6 + d$. The "true" orbit $\vec{r}_j(t)$ is linearized around $\vec{r}_{0j}(t)$, so that

$$\vec{r}_j(t) = \vec{r}_{0j}(t) + \sum_{i=1}^{6+d} \left. \frac{\partial \vec{r}_j(t)}{\partial p_{ij}} \right|_{p_{ij}=p_{0ij}} \cdot \Delta p_{ij} \ , \tag{5}$$

and the corrections $\Delta p_{ij} \doteq p_{ij} - p_{0ij}$ are the unknowns of a least-squares adjustment for all parameters, this time including the gravity field coefficients.

Using the positions, the observation equations read as

$$\mathbf{l}_{Pj} + \mathbf{v}_{Pj} = \mathbf{R}_j \,, \tag{6}$$

where $\mathbf{l}_{Pj}$ is the vector of the pseudo-observations, $\mathbf{v}_{Pj}$ are the residuals and

$$\mathbf{R}_j^T \doteq \left(\vec{r}_j^T(p_{ij}, t_1), \ldots, \vec{r}_j^T(p_{ij}, t_N)\right)$$

denotes the vector of the computed spacecraft positions $\vec{r}_j$ at the observation epochs $t_1, \ldots, t_N$, using the a priori gravity field and the selected background models. For the Ka-band range-rate (KBRR) observations we write in analogy

$$\mathbf{l}_K + \mathbf{v}_K = \frac{(\dot{\mathbf{R}}_2 - \dot{\mathbf{R}}_1) \cdot (\mathbf{R}_2 - \mathbf{R}_1)}{|\mathbf{R}_2 - \mathbf{R}_1|} \,, \tag{7}$$

where on the right-hand side are the magnitudes of the projections of the velocity differences onto the line of sight. Numerical integration of the equations of motion and of the variational equations allows us to express the right-hand side of the observation equations (6) and (7) and to set up the normal equation systems (NEQs) for both the position and KBRR observations.

These NEQs are set up on a daily basis. The position and KBRR NEQs are combined with an appropriate relative weight (see Sec. 3.2) and the daily combined NEQs are then stacked into weekly, monthly and eventually into a three-monthly NEQ, including the full PM phase. Arc-specific parameters are pre-eliminated prior to NEQ stacking and the accumulated three-monthly NEQ is eventually inverted to solve for the corrections of the SH coefficients w. r. t. the a priori gravity field coefficients. We do not apply any gravity field regularization.

Our approach for lunar gravity recovery has similarities with, but also differences compared to the approaches followed by the NASA groups. Table 1 shows a comparison of the CMA with the approach followed by the group at NASA Goddard Space Flight Center (GSFC), as detailed in Lemoine et al. (2013). Both approaches are relying on the estimation of empirical parameters. A total number of 42 (150) empirical parameters is estimated per day and satellite for the CMA when using a spacing of pseudo-stochastic pulses of 40 min (10 min). On the other hand, the GSFC approach uses, apart from solar radiation pressure scaling factors, around 72 (300) empirical acceleration parameters per day which are set up for each (quarter) orbital revolution. Moreover, each group is using its own stand-alone software package for the processing.

3. Initial orbit determination and modeling evaluation

In the first step of gravity field recovery, initial orbits are estimated based on a given a priori gravity field (see Sec. 2.2.1). Release 4 data for the KBRR from the Ka-band Lunar Gravity Ranging System (LGRS, Klipstein et al., 2013) are used along with GRAIL-A/B positions (GNI1B sub-product) to provide the a priori trajectories during the PM phase covering the period March-May 2012. All data are freely accessible via NASA's Planetary Data System[4] (Kahan, 2014).

Apart from yielding sufficiently accurate a priori orbits $\vec{r}_0(t)$ for the subsequent generalized orbit determination, this step is also useful for data screening (see Sec. 3.2) and for evaluating the quality of the force model. The analysis of KBRR residuals is in particular a useful technique to detect inconsistencies and problems in the data.

3.1. Fit of GNI1B positions

As in the case of the GRACE mission, the success of the GRAIL mission is based on highly accurate range-rate observations between the two satellites. However, since a complete orbit and gravity field determination from KBRR data alone is not possible (Rowlands et al., 2002), a sufficiently accurate a priori knowledge of the "absolute" trajectories of the two satellites is needed.

[4]PDS, `http://pds-geosciences.wustl.edu/missions/grail/default.htm`

	CMA	GSFC
Arc length	1 d	1 d – 2.5 d
Data processed	KBRR + GNI1B	KBRR + Doppler
Weighting of data	Fixed, $1:10^8 - 1:10^{10}$	Variance component estimation
Non-grav. force models	–	Solar and planetary radiation pressure
Arc parameters	Initial state, empirical acc., pulses, Ka-band time bias	Initial state, empirical acc., KBRR bias, Ka-band time bias, rad. pressure scaling factors
Global parameters	SH coefficients for $2 \leq l \leq 200$	SH coefficients for $2 \leq l \leq 900$, GM_M, Love numbers
Empirical acc.	1/rev in R/S/W, for whole day, unconstrained	Const. and 1/rev in S/W, for every (quarter) revolution, pair-wise exponential constraining
Pulses	Every 15-40 min in R/S/W, constr. to zero with 0.1 m/s sigma	–
Solution method	Gauss-Newton least-squares adjustment, all within the Bernese GNSS software	Gauss-Newton least-squares adjustment and QR factorization, GEODYN and standalone software
SH coeff. constraints	–	Kaula constr. for $l > 330$ (GRGM660PRIM) or $l > 600$ (GRGM900C)

Table 1: Comparison of CMA and gravity recovery approach used by NASA GSFC team.

Model	Radial	Along-track	Cross-track
JGL165P1	0.4172 ± 1.4102	-0.0035 ± 0.5963	-0.2201 ± 1.3513
SGM150J	-0.2339 ± 1.3881	-0.0020 ± 0.5287	-0.2208 ± 1.6016
GRGM900C	0.0210 ± 0.0227	0.0001 ± 0.0090	-0.2157 ± 0.1288

Table 2: Mean values and standard deviations of estimated pseudo-stochastic pulses for GRAIL-A over the entire PM phase, obtained in a GNI1B fit using different background gravity field models. Values in mm/s.

In the present study, the GNI1B positions are used as pseudo-observations for this purpose. Although they are not original observations, their usage allows us to adapt the CMA from GRACE — where GPS-derived kinematic positions of the probes are available (Jäggi et al., 2012) — to GRAIL, without the necessity of processing Doppler data from DSN tracking (see Sec. 5).

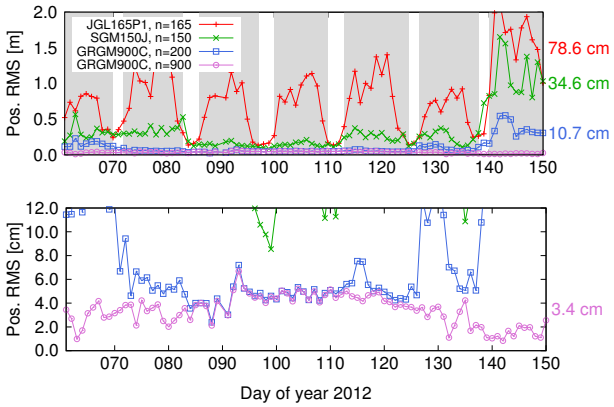

Figure 1: Daily RMS values of the position residuals for GRAIL-A over the entire PM phase (screened data). The bottom figure is a zoom of the top figure. The numbers at the right-hand side are the mean RMS values. The shaded areas mark the time spans during which less than 80 % of the probe orbit was visible from the Earth.

Figure 1 shows the daily RMS values of the GRAIL-A position residuals for the initial orbits generated for the whole PM phase using the GNI1B positions only, along with several background gravity fields; from the rather old Lunar Prospector model JGL165P1 (Konopliv et al., 2001), the Selene/Kaguya model SGM150J (Goossens et al., 2011), up to the recent GRGM900C GRAIL model. Pseudo-stochastic pulses are estimated every 40 minutes to compensate for the missing modeling of non-gravitational accelerations, e. g., caused by solar radiation pressure. The accuracy of the resulting orbital fits strongly depends on the background gravity field, especially on the far-side of the Moon. The gray areas in Fig. 1 indicate the time spans during which less than 80 % of the GRAIL orbits were visible from the Earth and thus the spacecraft were probing the far-side of the Moon. For Lunar Prospector, the lack of Doppler observations resulted in a particularly poor gravity field determination on the far-side, which manifests itself in position residuals up to several meters on these days. On the other hand, consistently using the recent GRGM900C model up to degree 900 as background gravity field results in an RMS of a few cm. The impact of using the full model GRGM900C is particularly large for the first and last days of the PM phase, when the GRAIL orbits were more eccentric and had a lower periapsis (see detail in the lower part of Fig. 1).

Table 2 contains the mean values and the standard deviations of the estimated pseudo-stochastic pulses for GRAIL-A over the entire PM phase (in mm/s). The pulses are obviously larger in radial and along-track directions when using the pre-GRAIL gravity models, while in the cross-track direction only a change in their variability is observed. Figure 2 shows the pulses for GRAIL-A over the entire PM phase, together

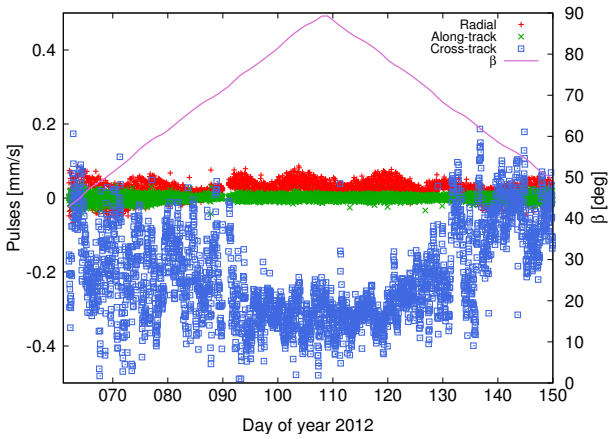

Figure 2: Estimated pulses (40 minutes spacing) for GRAIL-A in radial, along-track, and cross-track direction over the entire PM phase. GRGM900C up to degree 900 was used as background gravity field. The solid line shows the β-angle, the elevation of the Sun above the orbital plane.

with the β-angle, the elevation of the Sun above the orbital plane. The full model GRGM900C was used as background field. The pulses show a clear dependence on the β-angle, in particular in the cross-track direction, indicating that they (partially) compensate the accelerations induced by solar radiation pressure.

3.2. Combined fit of GNI1B positions and KBRR data

The addition of the KBRR observations further improves the a priori orbits and, more importantly, yields KBRR residuals, serving as a sensitive tool for modeling and data quality assessment. KBRR observations provide the relative velocity of the two GRAIL probes along the line of sight with a nominal accuracy of about $0.05\,\mu$m/s (Lemoine et al., 2013). With the GNI1B positions not being original observations and because we lack information on their accuracy, the relative weighting of the two observation types is not straightforward. One approach could be to consider the relative fit accuracies of roughly 1 cm for the GNI1B positions (see Fig. 1) and $1\,\mu$m/s for the KBRR (see Fig. 3), which would suggest a relative weighting of the two observation types of $1 : 10^8$ (ratio of the squares of the two accuracies). However, the actual orbital position accuracy is probably less, while the KBRR are more accurate, suggesting relative weightings of $1 : 10^{10} - 1 : 10^{12}$. The impact of the weighting on the gravity field solution will be discussed in Sec. 4.2. Currently, for a given solution shown here we use a fixed ratio for all days. A more sophisticated weighting, like variance-component estimation (Koch and Kusche, 2002) might be applied in the future, when GNI1B positions will be replaced by Doppler observations.

KBRR residuals can be used for screening the Ka-band data in the framework of the initial orbit determination. With the existing high-quality GRAIL gravity fields at hand this can be efficiently done by computing orbits $\vec{r}_0(t)$ based on, e.g., GRGM900C as background gravity field model and by using both the GNI1B positions and the KBRR observations. The resulting KBRR residuals are checked for outliers to identify portions of the KBRR data to be removed from the processing.

Figure 3 shows the daily RMS values for the KBRR residuals over the entire PM phase for a combined (GNI1B positions and KBRR observations) initial orbit determination. When using the full model GRGM900C as background gravity field, the KBRR residuals are at the μm/s level, as shown in detail in Figure 4 for the first 200 minutes of day 062 (2 March 2012). The horizontal bars indicate the time spans during which the GRAIL probes are in sunlight (GRAIL-A on top, GRAIL-B at the bottom). At the transitions between light and shadow each of the probes experiences different illumination conditions, resulting in significant changes in the KBRR residuals. This indicates that missing solar radiation pressure is now the largest shortcoming of our modeling. This is partially compensated by equally spaced pseudo-stochastic pulses, whose impact every 40 minutes (indicated by the vertical lines) is also clearly visible. A possible

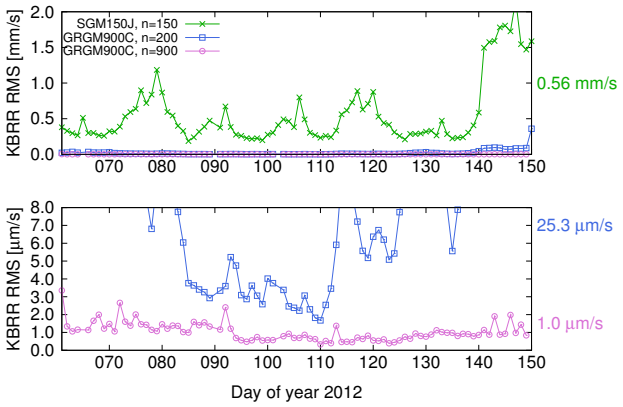

Figure 3: Daily RMS values of KBRR residuals over the entire PM phase (screened data). The bottom figure is a zoom of the top figure. The numbers at the right-hand side are the mean RMS values.

further improvement would be to estimate additional pulses at transitions between light and shadow, which we did not consider.

Hence, even without a sophisticated modeling of non-gravitational forces, the chosen set of empirical accelerations and pseudo-stochastic pulses allows to get down to a comfortable residual level.

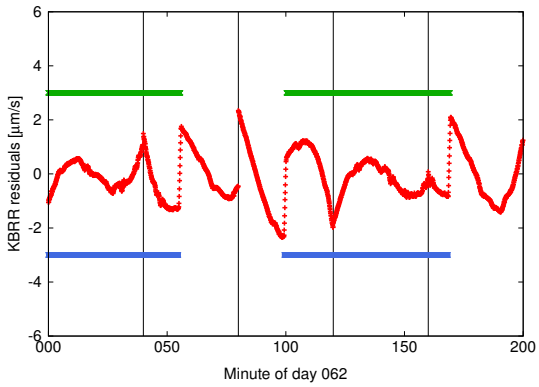

Figure 4: KBRR residuals for the first 200 minutes of day 062. Horizontal bars: time spans during which the GRAIL probes are in sunlight (GRAIL-A on top, GRAIL-B at the bottom). Vertical lines: times where pseudo-stochastic pulses are applied.

3.3. Comparison of release 2 and release 4 data

The results presented in this paper are based on release 4 data (published on 1 April 2014). Nevertheless, we started this study working on release 2. Based on the lessons learned, we point out some useful aspects for handling this data.

KBRR data result from a complex iterative processing of the inter-satellite Ka-band phase measurements which are corrected for several effects (geometric, time-of-flight, clock offsets, ...), as detailed in Kruizinga et al. (2013). The observation epochs for the Ka-band range data (as well as for the GNI1B positions) are generally given in the barycentric dynamical time (TDB) frame as seconds past 12:00:00, 1 January 2000 (Kahan, 2014). Our attempts to reduce the KBRR residuals using release 2 data showed that the

introduction of a Ka-band time bias, i. e., an offset of the actual observation epoch from the nominal one (already mentioned in Lemoine et al. (2013)), was necessary. Allowing for such an offset greatly reduced the KBRR residuals, as shown in Fig. 5.

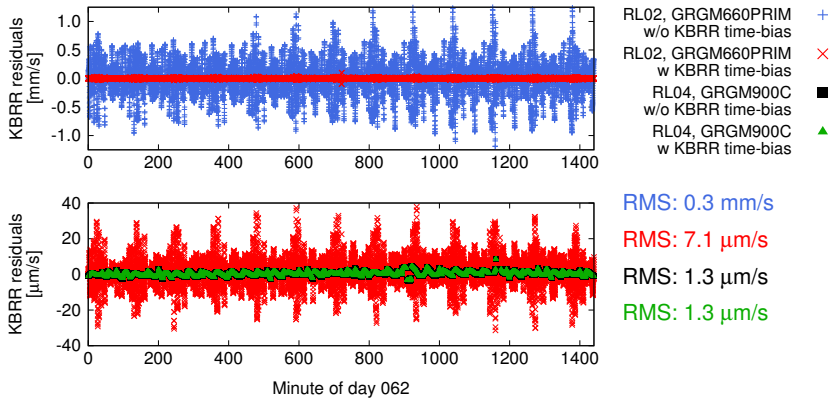

Figure 5: KBRR residuals for day 062, using release 2 data together with GRGM660PRIM and release 4 data together with GRGM900C, with and without KBRR time-bias. Note that the scales are different for the top and bottom figure.

For the release 2 data of the PM phase the estimated time bias turned out to oscillate around a mean value of -1.02 s with a period of about one month and a peak-to-peak value of about 10 ms, as illustrated in Fig. 6. The release 2 data of the EM phase did not show such large Ka-band time biases. Release 4 of the data does not show large Ka-band time offsets for the PM phase either (as stated by Lemoine et al. (2014)). In this case, the estimation of a Ka-band time bias has only a minor impact on both the KBRR residuals and on the gravity field solution (see Sec. 4.4).

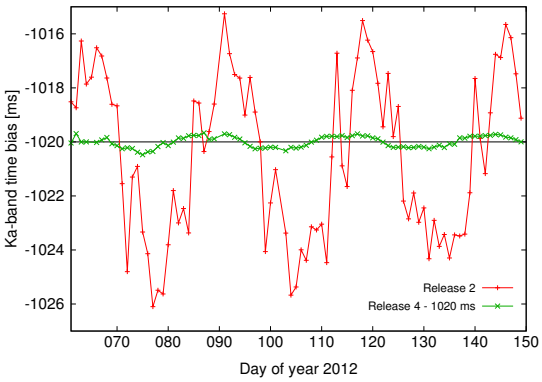

Figure 6: The estimated Ka-band time bias when using release 2 data together with GRGM660PRIM and release 4 data together with GRGM900C (shifted by -1020 ms).

Figure 5 also illustrates the improvement between the two data releases. Even when estimating a Ka-band time bias, the KBRR residuals obtained from release 2 data are nearly an order of magnitude larger than the residuals obtained from release 4 data. Furthermore, the very dominant once-per-revolution signals in the residuals are significantly reduced when passing from release 2 to release 4 of the data.

4. Gravity field recovery

The initial orbits are now used as a priori orbits for the actual gravity field recovery. As explained in Sec. 2.2.2, the recovery is designed as a generalized orbit determination process, in which both the orbits and the gravity field are improved together. In this section, we first discuss the spacing of the pseudo-stochastic pulses, analyze the impact of the relative weighting of position and KBRR data on the solution, and demonstrate the performance of the CMA regarding the independence of the final gravity field solutions from the a priori field. We then compare gravity field solutions obtained from releases 2 and 4 of the data, before presenting and evaluating our first lunar gravity field solutions up to degree and order 200. For a common comparison of different gravity fields, we will often make use of the difference degree amplitude

$$\Delta_l = \sqrt{\frac{1}{2l+1} \sum_{m=0}^{l} \left(\Delta\bar{C}_{lm}^2 + \Delta\bar{S}_{lm}^2 \right)} \,, \tag{8}$$

where $\Delta\bar{C}_{lm}$ and $\Delta\bar{S}_{lm}$ are the differences between the corresponding SH coefficients of the tested fields. Analogously, we will show the signal and error degree amplitudes, where in Eq. (8) $\Delta\bar{C}_{lm}$ and $\Delta\bar{S}_{lm}$ are replaced by the values of the coefficients and their errors, respectively.

4.1. Spacing of pseudo-stochastic pulses

Since at the time being we do not explicitly model any non-gravitational forces, the setting up of pseudo-stochastic pulses is crucial to absorb model deficiencies. While on one hand a higher number of pulses allows for better fits of the observations, too many pulses may absorb gravity field signal to be recovered (Jäggi et al., 2012). To find an appropriate parametrization, a number of gravity field solutions up to degree and order 120 were computed, differing in the amount of pulses. The comparison of these solutions w. r. t. GRGM900C (in terms of difference degree amplitudes, see Eq. (8)) showed that a spacing of around 30-40 minutes between pulses is the optimum. This holds, if no gravity field information is introduced beyond degree 120. On the other hand a high-quality a priori gravity field like GRGM900C can be introduced to high degrees. Adjusting only the coefficients up to degree 120, but keeping fixed the coefficients beyond degree 120 reduces the omission errors (i.e., the errors due to a finite expansion of the potential) and demonstrates the precision of the solution we could obtain at best if we estimated the SH coefficients to higher degrees. In this case, a smaller spacing between the pseudo-stochastic pulses (around 15 minutes) turns out to be more helpful, since the solution is more sensitive to model deficiencies and not dominated by omission errors.

In the case of Earth gravity recovery the spacing of the pseudo-stochastic pulses can be straightforwardly chosen based on a trade-off between a compensation of model deficiencies and a degradation of the gravity field solution due to too many pulses. However, due to the much slower rotation of the Moon, consecutive GRAIL satellite ground tracks are much closer to each other (at the equator about 30 km for GRAIL compared to about 2500 km for GRACE) and a uniform pulse spacing can cause a very systematic selenographic distribution of the locations where the pulses are applied, introducing a resonance-like degradation of the gravity field solution. Figure 7a shows the difference and error degree amplitudes of three degree-120 solutions which were obtained with different pulse spacings and using the model GRGM900C up to degree and order 660 as a priori field. A relative weighting of $1 : 10^8$ for positions and KBRR data was used. For the 40 and 30 minutes solution one can notice a clear increase of the differences at degrees around 55 and 75, respectively. For the 10 minutes solution a degradation appears only above degree 120. Fig. 7b shows the selenographic positions where the 40 minutes and 30 minutes pulses were applied for GRAIL-A. Both spacings show a rather regular distribution of the pulses over the lunar surface; the pattern for 10 minutes spacing resembles the 40 minutes pattern but is more closely meshed. As in the case of orbit resonances, these systematic patterns degrade coefficients of given orders (see also Fig. 12), causing the noticeable increases in the difference degree amplitudes. For the degree-200 solution AIUB-GRL200B, which is based on GRGM900C up to degree 660 (see Sec. 4.5), the pulse spacing was set to 15 minutes. This results in a slightly less regular distribution of the pulses, but the effect is still present. We point out that the mentioned issue is a rather small effect that only becomes obvious if the omission errors are significantly reduced by introducing a GRAIL a priori field up to a high degree.

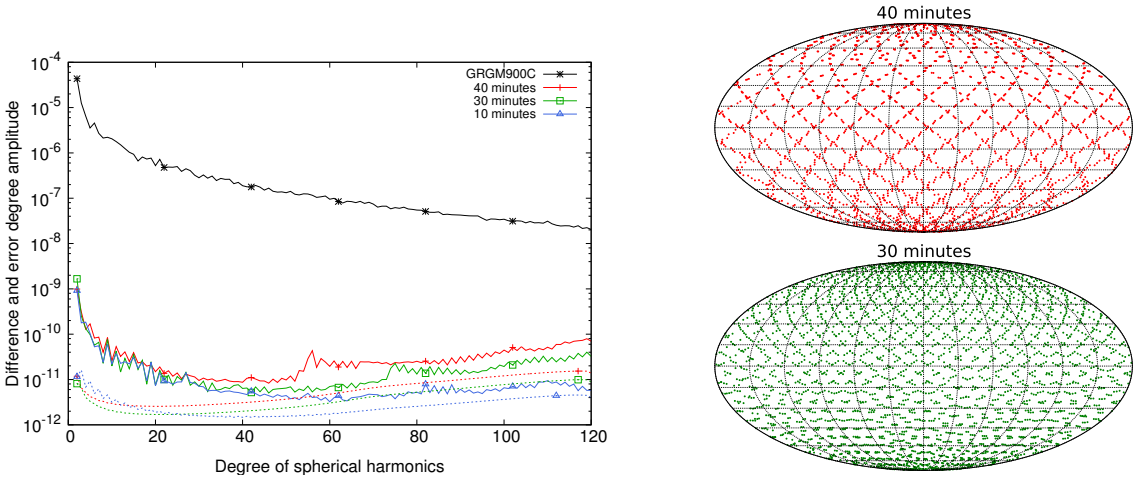

(a) (b)

Figure 7: (a): Difference degree amplitudes of solutions that were obtained with a spacing of 40, 30 and 10 minutes between pseudo-stochastic pulses, respectively. GRGM900C was used as a priori field up to degree 660. Dotted lines: formal errors. (b): Selenographic locations where the pulses were applied to GRAIL-A with a pulse spacing of 40 minutes (top) and 30 minutes (bottom), respectively (over full PM phase, Mollweide projection centered around 0°).

4.2. Relative weighting of positions and KBRR data

As discussed in Sec. 3.2, we set up the (fixed) relative weighting in the combination of the GNI1B positions and KBRR data based on their accuracy. Depending on what is taken as accuracy measure, weighting ratios of $1 : 10^8 - 1 : 10^{12}$ are reasonable. Figure 8 shows the difference and error degree amplitudes of degree-120 solutions which were obtained by introducing GRGM900C up to degree and order 660 and by using a 10 minutes spacing of the pseudo-stochastic pulses. The solutions only differ by the relative weighting between position and KBRR data.

While the differences w. r. t. GRGM900C are similar for the solutions with a weighting of $1 : 10^8$ and $1 : 10^{10}$, a value of $1 : 10^{12}$ obviously degrades the solution. Regarding the formal errors (dashed lines), the solution with a weighting of $1 : 10^{10}$ is preferred over the $1 : 10^8$ solution. In the following sections, we will present gravity field solutions which are based on a relative weighting of either $1 : 10^8$ or $1 : 10^{10}$.

4.3. Independence of the solution from the a priori field

The independence of the final solution from the a priori gravity field is a crucial aspect of gravity field recovery. Figure 9 shows the difference degree amplitudes of degree-120 solutions based on different a priori fields w. r. t. GRGM900C. When starting with JGL165P1 truncated to d/o 120, two iterations are sufficient to reach the level of a solution obtained from GRGM900C after one iteration (dashed line). A pulse spacing of 40 minutes and a relative weighting of $1 : 10^8$ between GNI1B positions and KBRR data was used. Moreover, since we do not solve for the degree 0 of the selenopotential (GM_M), one constant empirical acceleration in radial direction was additionally estimated per day.

4.4. Comparison of release 2 and release 4 data

In analogy to the discussion presented in Sec. 3.3, Fig. 10 shows difference and error degree amplitudes of gravity field solutions obtained from release 2 and release 4 of the position and Ka-band data and the impact of the estimation of a Ka-band time bias. The solutions are all estimated up to d/o 120 and use GRGM900C up to d/o 120 as a priori field, with a relative weighting of $1 : 10^8$ and a pulse spacing of 40 minutes.

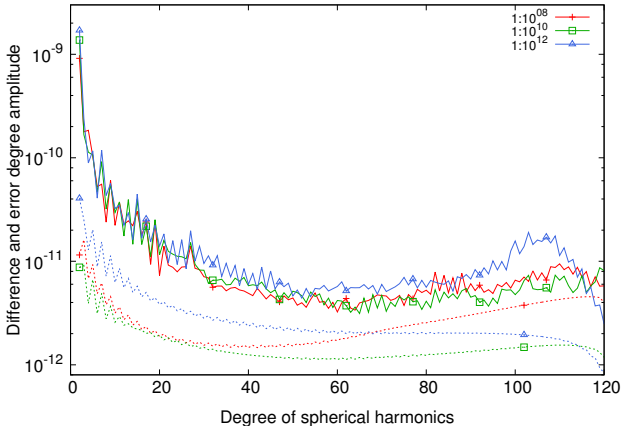

Figure 8: Difference degree amplitudes (w. r. t. GRGM900C) of solutions obtained with different relative weighting between position and KBRR data. Dotted lines: formal errors.

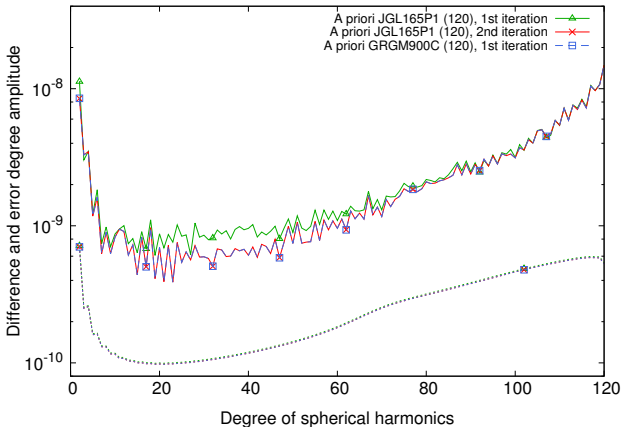

Figure 9: Difference degree amplitudes (w. r. t. GRGM900C) of solutions obtained from different a priori fields. Starting with the comparably low-performing field JGL165P1 (truncated at degree 120) two iterations are sufficient to derive a solution very similar to the one obtained after one iteration from GRGM900C, resolved up to d/o 120. Dotted lines: formal errors.

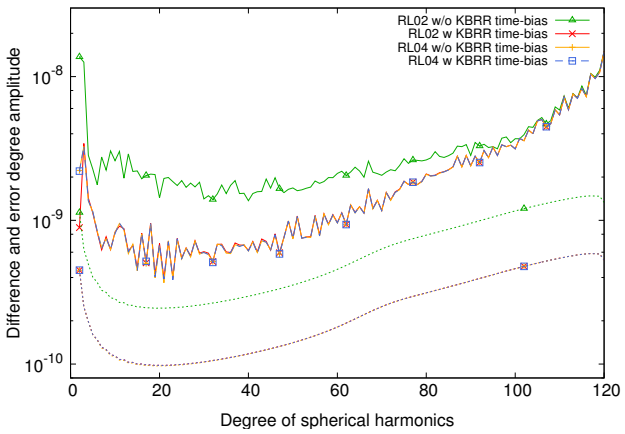

Figure 10: Difference degree amplitudes (w. r. t. GRGM900C) of estimated solutions using release 2 and release 4 data, with and without KBRR time-bias. Dotted lines: formal errors.

Allowing for a Ka-band time bias significantly improves the gravity field solution when using release 2 data. On the other hand, at least at our current level of accuracy, taking into account a Ka-band time bias is less critical for release 4 data. This is in agreement with the fact that, for release 4 data, the estimated Ka-band time bias is very small and that the KBRR residuals are almost unaffected by this parameter (see Sec. 3.3).

Figure 5 showed that the KBRR residuals are considerably smaller when using release 4 data with or without Ka-band time bias instead of release 2 data with Ka-band time bias. The corresponding gravity field solutions appear to differ only at the lowest degree. Interestingly, for degree 2 the agreement with GRGM900C is better for the gravity field solution obtained from release 2 data and including a time bias than for the solutions obtained from release 4 data.

4.5. First gravity field solutions to d/o 200

Based on the results of the above experiments and using the parametrization described in Sec. 2.2, we computed degree-200 solutions based on release 4 data of the PM phase.

Figure 11 shows the difference degree amplitudes of the estimated degree-200 solutions w. r. t. GRGM900C. The AIUB-GRL200A curve represents a solution which was obtained using GRGM900C up to d/o 200 as a priori field, i. e., by not making use of it beyond the maximum degree resolved. This solution was obtained after one iteration. In order to stress the independence of our solution from the a priori field, we also show a degree-200 solution computed by using JGL165P1 within two iterations (dashed curve). This solution very closely matches AIUB-GRL200A. Both solutions were obtained using a 40 minutes spacing of the pseudo-stochastic pulses and with a relative weighting of $1 : 10^8$ between GNI1B and KBRR data. Furthermore, because we do not solve for GM_M, one constant empirical radial acceleration per day was estimated. For reference, the difference degree amplitudes of JGL165P1, SGM150J and of the JPL GRAIL field GL0900C are shown, as well. The dotted lines indicate the formal errors of the respective solutions.

To assess the importance of KBRR data for the gravity field solution, a position-only solution to d/o 200 was computed using GRGM660PRIM up to d/o 200 as a priori field and a pulse spacing of 40 minutes. We point out that this solution does not coincide with a Doppler-only solution, since the GNI1B positions are continuous and contain both Doppler and KBRR information. Its difference degree amplitude suggests that AIUB-GRL200A is dominated by the GNI1B positions only at the lowest degrees. The inclusion of the KBRR data strongly improves the solution and reduces the formal errors over almost the entire spectral domain.

In order to reduce the omission errors, GRGM900C was also used up to d/o 660 as the a priori field, resulting in a solution represented by the AIUB-GRL200B curve. A 15 minutes spacing of the pseudo-

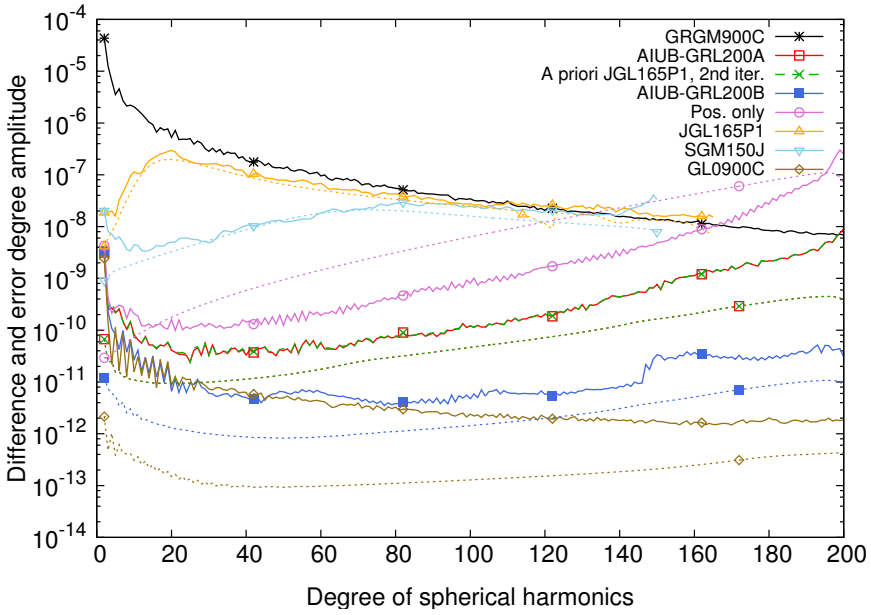

Figure 11: Difference degree amplitudes of estimated degree-200 solutions, of two pre-GRAIL solutions and of GL0900C. AIUB-GRL200A: the a priori field (GRGM900C) was used up to d/o 200. Dashed: solution when starting from JGL165P1 after two iterations. AIUB-GRL200B: the a priori field (GRGM900C) was used up to d/o 660 to reduce the omission errors. Pos. only: a position-only solution (using GRGM660PRIM to degree 200 as a priori field), showing that KBRR observations improve the solution over nearly the full spectral domain. Dotted lines: formal errors.

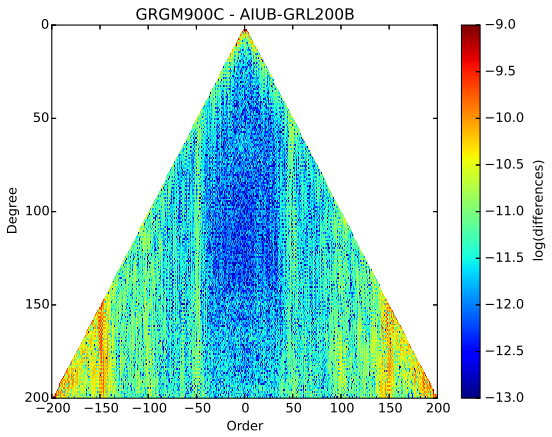

Figure 12: Coefficient differences between solutions GRGM900C and AIUB-GRL200B.

stochastic pulses and a relative weighting of $1 : 10^{10}$ was used. For consistency reasons, one constant empirical radial acceleration per day was estimated for this solution as well. This result indicates the precision that could be currently achieved at best when estimating gravity field coefficients beyond d/o 200 and shows the potential of our approach for the perspective development of a GRAIL solution to higher degrees. It is remarkable to note that the differences of this solution are comparable to the differences w. r. t. the JPL GRAIL field GL0900C up to degree 50. We point out that also AIUB-GRL200B results from a single iteration.

The AIUB-GRL200B solution shows a sudden increase of differences w. r. t. GRGM900C around degree 150. We attribute this to the spatial distribution of the pseudo-stochastic pulses discussed in Sec. 4.1. Figure 12 shows the coefficient differences between GRGM900C and AIUB-GRL200B. It reveals that the increase in the difference degree amplitude originates from degraded coefficients of orders around 150. The coefficients of orders around 50 and 100 are (less) degraded as well. This resembles the problems observed in gravity field recovery from satellites showing orbit resonances — see, e.g., (Wagner et al., 2006) for a discussion of orbit resonances for GRACE. Options to overcome these limitations are a more adequate choice of a uniform pulse spacing, the usage of non-uniform spacings, or, eventually, an explicit modeling of non-gravitational accelerations, rendering the use of pseudo-stochastic pulses dispensable or at least less crucial.

Introducing AIUB-GRL200A as background gravity field for a postfit of the KBRR data (with 40 minutes pulse spacing) yields a mean RMS of 19.7 μm/s, which is slightly smaller than the RMS obtained when using GRGM900C truncated at degree 200 (see Fig. 3). If the postfit is performed with a gravity field consisting of AIUB-GRL200B for the first 200 degrees and of GRGM900C for degrees 201–660, the mean RMS value is 1.1 μm/s when using pulses every 40 minutes, and 0.7 μm/s when using pulses every 15 minutes.

Figure 13 shows the free-air gravity anomalies (Heiskanen and Moritz, 1967) derived from AIUB-GRL200A using a Moon reference radius of 1738 km. It shows many details which can be correlated with surface features and it does not show the asymmetry in resolution between near- and far-side which was characteristic for all pre-GRAIL gravity field solutions.

4.6. Correlation between gravity and topography

As a further validation of our results, we computed the correlation between gravity and topography (Wieczorek, 2007). Using the lunar topography derived from the Lunar Orbiter Laser Altimeter (LOLA, Smith et al., 2010) in its spherical harmonics representation[5] and following the procedure outlined by Wieczorek

[5]See the "MoonTopo2600pa" shape model by Mark Wieczorek at `http://www.ipgp.fr/~wieczor/SH/SH.html`

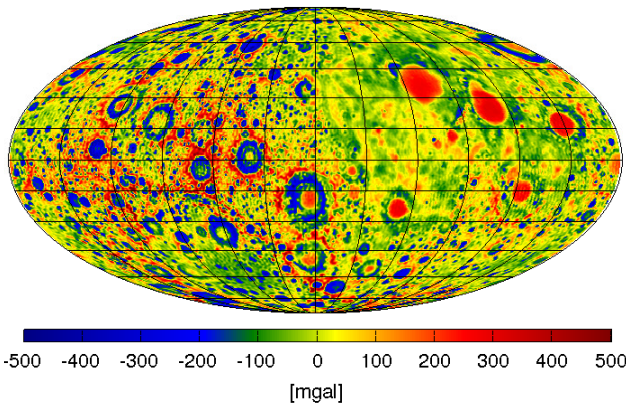

Figure 13: Free-air gravity anomalies of AIUB-GRL200A on a $0.5° \times 0.5°$ grid (Mollweide projection centered around 270°, with the nearside on the right).

and Phillips (1998), we computed the topography-induced gravity. We assumed an overall density of $2560\,\mathrm{kg/m^3}$ (Lemoine et al., 2013) and we used the expansion of the topography (height w. r. t. the reference radius) up to the 9th power. Let $S_{gg}(l)$ and $S_{hh}(l)$ be the power spectrum of the gravity field and of the topography-induced gravity field, and $S_{gh}(l)$ their cross-power spectrum at degree l. The correlation $\gamma(l)$ at degree l, shown in Fig. 14, is then computed as

$$\gamma(l) = \frac{S_{hg}(l)}{\sqrt{S_{hh}(l) S_{gg}(l)}} \,. \tag{9}$$

Figure 14 shows that the correlation for our solution AIUB-GRL200A is comparable to the correlation for GRGM900C up to degree 170, where it drops below 0.98. The decrease for higher degrees is mainly due to the omission errors. The correlation for AIUB-GRL200B does not drop below 0.989 up to degree 200 and closely matches the correlations for GRGM900C (see detail in lower part of Fig. 14).

5. Outlook and perspectives

Our results demonstrate the potential of a relatively straightforward adaption of the CMA from GRACE to GRAIL for the recovery of the lunar gravity field. Nevertheless, several improvements are foreseen in view of a higher-resolved AIUB solution. First, direct and indirect solar radiation pressure should be dealt with in a more physical way by using a macro model of the GRAIL probes. In addition, a thorough test of more sophisticated empirical orbit models will be conducted. Also, a more refined data screening, and a precise modeling of orbital maneuvers — mainly angular momentum desaturation maneuvers (Konopliv et al., 2013) — might increase the amount of processed data and improve the solution.

Moreover, the use of the GNI1B position data as pseudo-observations is not fully satisfactory and is potentially dangerous for the orbit and gravity field determination (Jäggi et al., 2015). Besides the KBRR observations, GRAIL has been regularly Doppler tracked by several Earth-based stations of the DSN. The tracking took place using both X-band and S-band communications, with a nominal accuracy of 0.03 mm/s and 0.1 mm/s, respectively. In terms of Doppler frequency, this roughly corresponds to 1 mHz accuracy.

We are currently improving the Doppler modeling in the Bernese GNSS software in order to reach the nominal accuracy as well as setting up the orbit improvement based on DSN observations. The outcome of this development will be addressed in a future work focusing on the end to end analysis of the lunar gravity field starting from original observed data within the Bernese GNSS software, which is necessary to obtain fully independent solutions for both orbit and gravity field determination.

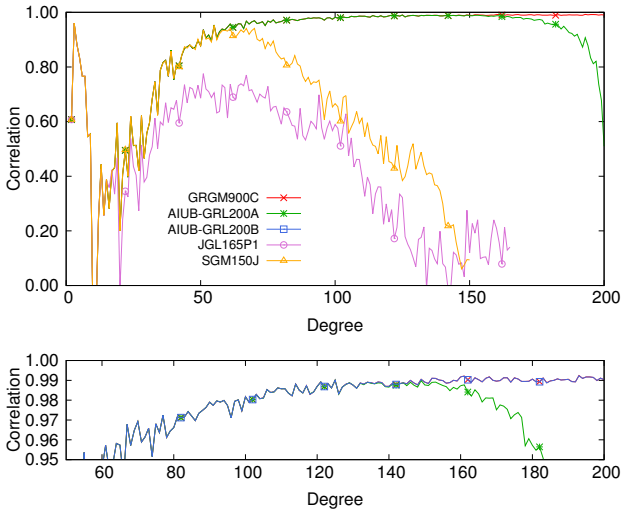

Figure 14: Correlations between the gravity field induced by LOLA topography and several lunar gravity field solutions.

6. Summary and conclusion

The ultra-precise inter-satellite ranging measurements of the GRAIL mission allow for impressive major improvements in lunar gravity field recovery. Given the similarities between the Moon-orbiting GRAIL mission and the Earth-orbiting GRACE mission it is natural to seek for an adaption of our gravity recovery approach — the CMA — from GRACE to GRAIL. The availability of the GNI1B positions of the GRAIL probes allows us to directly initiate this task within the Bernese GNSS software without first having to process DSN Doppler data.

After having outlined the principles of the CMA, we have first focused on results from the initial orbit determination. We have pointed out differences between release 2 and release 4 data and have shown that it is mandatory to estimate a Ka-band time bias when processing release 2 data. We have demonstrated that we reach the few cm level for position residuals and the 1 μm/s level for the KBRR residuals when using release 4 data together with the GRGM900C gravity field model. This result can be achieved even without a sophisticated modeling of non-gravitational forces by using an adequate orbit parametrization in terms of a limited number of empirical accelerations and pseudo-stochastic pulses. We have analyzed the impact of the spacing of the pseudo-stochastic pulses on the gravity field solutions, showing that an inappropriate spacing can lead to resonance-like degradations. Moreover, we have studied the influence of the relative weighting of GNI1B positions and KBRR data on the gravity field solution and we have demonstrated the independence of our gravity recovery approach from the a priori field.

We have presented the lunar gravity field models AIUB-GRL200A and AIUB-GRL200B up to degree and order 200. They use GRGM900C as a priori field (up to degree and order 200 and 660, respectively), are estimated without applying any constraints and within one single iteration. As further validation, a degree-200 solution based on Lunar Prospector JGL165P1 as a priori gravity field was also presented and shown to converge on AIUB-GRL200A within two iterations. Although not completely independent from the official GRAIL solutions (due to the usage of the GNI1B positions), AIUB-GRL200A/B represent alternative solutions for the lunar gravity field from GRAIL data obtained by using an independent software and exceeding the GRAIL mission requirements (Konopliv et al., 2013). We have compared our solutions to the GRAIL solutions GRGM900C and GL0900C, showing that the discrepancies among AIUB-GRL200B and the two NASA models are already comparable, at least up to d/o 50. Moreover, we have evaluated our solutions in terms of the correlations to the LOLA topography-induced gravity fields. For AIUB-GRL200A

the correlation drops below 0.98 at degree 170, for AIUB-GRL200B it does not drop below 0.98 up to degree 200.

Both models, AIUB-GRL200A and AIUB-GRL200B, are available at the web page of the International Centre for Global Earth Models (ICGEM, `http://icgem.gfz-potsdam.de`).

Although convenient for the initialization of GRAIL data processing, the use of the GNI1B positions is not completely satisfactory. The implementation of DSN Doppler data processing into the Bernese GNSS Software will eventually allow us to contribute a fully stand-alone solution. Furthermore, the addition of the data at lower orbital altitude from the EM phase, as well as explicit modeling of solar radiation pressure will strengthen future solutions with higher resolution.

Acknowledgements

We are grateful to Frank Lemoine, Alex Konopliv, Sander Goossens, Gerhard Kruizinga and Ulrich Meyer for fruitful discussions. Moreover, we thank the two reviewers for their valuable comments and remarks. GRAIL inter-satellite Ka-band and DSN tracking data was obtained from the Planetary Data System (PDS). This study has been funded with the support of the Swiss National Science Foundation (project "A Bernese Gravity Field Model of the Moon" with number 200021_146512).

References

Asmar, S. W., Konopliv, A. S., Watkins, M. M., Williams, J. G., Park, R. S., Kruizinga, G., Paik, M., Yuan, D.-N., Fahnestock, E., Strekalov, D., Harvey, N., Lu, W., Kahan, D., Oudrhiri, K., Smith, D. E., Zuber, M. T., Sep. 2013. The scientific measurement system of the Gravity Recovery and Interior Laboratory (GRAIL) mission. Space Science Reviews 178, 25–55.

Beutler, G., 2005. Methods of Celestial Mechanics. Springer Berlin Heidelberg.

Beutler, G., Jäggi, A., Mervart, L., Meyer, U., Oct. 2010. The celestial mechanics approach: theoretical foundations. Journal of Geodesy 84, 605–624.

Dach, R., Beutler, G., Bock, H., Fridez, P., Gäde, A., Hugentobler, U., Jäggi, A., Meindl, M., Mervart, L., Prange, L., Schaer, S., Springer, T., Urschl, C., Walser, P., 2007. Bernese GPS Software - Version 5.0. Astronomical Institute, University of Bern.

Fahnestock, E. G., Park, R. S., Yuan, D. N., Konopliv, A. S., 2012. Spacecraft thermal and optical modeling impacts on estimation of the GRAIL lunar gravity field. AIAA/AAS Astrodynamics Specialist Conference, Minneapolis, Minnesota, August 13-16, 2012.

Folkner, W. M., Williams, J. G., Boggs, D. H., Aug. 2009. The planetary and lunar ephemeris DE 421. Interplanetary Network Progress Report 178, C1.

Goossens, S., Matsumoto, K., Ishihara, Y., 2011. Improved High-Resolution Lunar Gravity Field Model From SELENE and Historical Tracking Data. In: AGU Fall Meeting, Abstract P44B-05.

Heiskanen, W. A., Moritz, H., 1967. Physical geodesy. San Francisco : W. H. Freeman.

Jäggi, A., Beutler, G., Mervart, L., Hugentobler, U., 2008. Precise orbit determination for GRACE using GPS and K-band data. In: 37th COSPAR Scientific Assembly.

Jäggi, A., Beutler, G., Meyer, U., Bock, H., Mervart, L., 2015. The role of position information for the analysis of K-band data: Experiences from GRACE and GOCE for GRAIL gravity field recovery. International Association of Geodesy Symposia. Springer Berlin Heidelberg, pp. 1–7.
URL `http://dx.doi.org/10.1007/1345_2015_63`

Jäggi, A., Beutler, G., Meyer, U., Prange, L., Dach, R., L., M., 2012. AIUB-GRACE02S – Status of GRACE Gravity Field Recovery using the Celestial Mechanics Approach. Geodesy for Planet Earth 136, 161–170, edited by S. Kenyon, M.C. Pacino, and U. Marti.

Jäggi, A., Hugentobler, U., Beutler, G., 2006. Pseudo-Stochastic Orbit Modeling Techniques for Low-Earth Orbiters. Journal of Geodesy 80, 47–60.

Kahan, D., 2014. GRAIL Data Product Software Interface Specification. JPL D-76383, Version 1.6. Tech. rep., California Institute of Technology.

Klinger, B., Baur, O., Mayer-Gürr, T., Feb. 2014. GRAIL gravity field recovery based on the short-arc integral equation technique: Simulation studies and first real data results. Planetary and Space Sciences 91, 83–90.

Klipstein, W. M., Arnold, B. W., Enzer, D. G., Ruiz, A. A., Tien, J. Y., Wang, R. T., Dunn, C. E., Sep. 2013. The Lunar Gravity Ranging System for the Gravity Recovery and Interior Laboratory (GRAIL) Mission. Space Science Reviews178, 57–76.

Koch, K.-R., Kusche, J., 2002. Regularization of geopotential determination from satellite data by variance components. Journal of Geodesy 76 (5), 259–268.
URL `http://dx.doi.org/10.1007/s00190-002-0245-x`

Konopliv, A. S., Asmar, S. W., Carranza, E., Sjogren, W. L., Yuan, D. N., Mar. 2001. Recent Gravity Models as a Result of the Lunar Prospector Mission. Icarus 150, 1–18.

Konopliv, A. S., Park, R. S., Yuan, D.-N., Asmar, S. W., Watkins, M. M., Williams, J. G., Fahnestock, E., Kruizinga, G., Paik, M., Strekalov, D., Harvey, N., Smith, D. E., Zuber, M. T., Jul. 2013. The JPL lunar gravity field to spherical harmonic degree 660 from the GRAIL Primary Mission. Journal of Geophysical Research (Planets) 118, 1415–1434.

Konopliv, A. S., Park, R. S., Yuan, D.-N., Asmar, S. W., Watkins, M. M., Williams, J. G., Fahnestock, E., Kruizinga, G., Paik, M., Strekalov, D., Harvey, N., Smith, D. E., Zuber, M. T., Mar. 2014. High-resolution lunar gravity fields from the GRAIL Primary and Extended Missions. Geophysical Research Letter41, 1452–1458.

Kruizinga, G., Asmar, S., Fahnestock, E., Harvey, N., Kahan, D., Konopliv, A., Oudrhiri, K., Paik, M., Park, R., Strekalov, D., Watkins, M., Yuan, D.-N., 2013. The role of GRAIL orbit determination in preprocessing of gravity science measurements. In: 23rd AAS/AIAA Spaceflight Mechanics Meeting, Kauai, Hawaii, February 10-14 2013. Pasadena, CA : Jet Propulsion Laboratory, National Aeronautics and Space Administration, 2013.

Lemoine, F. G., Goossens, S., Sabaka, T. J., Nicholas, J. B., Mazarico, E., Rowlands, D. D., Loomis, B. D., Chinn, D. S., Caprette, D. S., Neumann, G. A., Smith, D. E., Zuber, M. T., Aug. 2013. High-degree gravity models from GRAIL primary mission data. Journal of Geophysical Research (Planets) 118, 1676–1698.

Lemoine, F. G., Goossens, S., Sabaka, T. J., Nicholas, J. B., Mazarico, E., Rowlands, D. D., Loomis, B. D., Chinn, D. S., Neumann, G. A., Smith, D. E., Zuber, M. T., May 2014. GRGM900C: A degree 900 lunar gravity model from GRAIL primary and extended mission data. Geophysical Research Letter41, 3382–3389.

Moyer, 2003. Formulation for observed and computed values of Deep Space Network observables. Hoboken, NJ.

Pavlis, D. E., Wimert, J., McCarthy, J. J., 2013. GEODYN II system description. Tech. rep., SGT Inc., contractor report, vols. 1-5.

Petit, G., Luzum, B., 2010. IERS Conventions (2010). IERS Technical Note 36, 1.

Rowlands, D. D., Ray, R. D., Chinn, D. S., Lemoine, F. G., 2002. Short-arc analysis of intersatellite tracking data in a gravity mapping mission. Journal of Geodesy 76 (6-7), 307–316.
URL http://dx.doi.org/10.1007/s00190-002-0255-8

Smith, D. E., Zuber, M. T., Jackson, G. B., Cavanaugh, J. F., Neumann, G. A., Riris, H., Sun, X., Zellar, R. S., Coltharp, C., Connelly, J., Katz, R. B., Kleyner, I., Liiva, P., Matuszeski, A., Mazarico, E. M., McGarry, J. F., Novo-Gradac, A.-M., Ott, M. N., Peters, C., Ramos-Izquierdo, L. A., Ramsey, L., Rowlands, D. D., Schmidt, S., Scott, V.Stanley, I., Shaw, G. B., Smith, J. C., Swinski, J.-P., Torrence, M. H., Unger, G., Yu, A. W., Zagwodzki, T. W., 2010. The Lunar Orbiter Laser Altimeter investigation on the Lunar Reconnaissance Orbiter mission. Space Science Reviews 150 (1-4), 209–241.
URL http://dx.doi.org/10.1007/s11214-009-9512-y

Tapley, B. D., Bettadpur, S., Ries, J. C., Thompson, P. F., Watkins, M. M., Jul. 2004. GRACE Measurements of Mass Variability in the Earth System. Science 305, 503–506.

Wagner, C., McAdoo, D., Klokocnik, J., Kostelecky, J., 2006. Degradation of geopotential recovery from short repeat-cycle orbits: Application to GRACE monthly fields. Journal of Geodesy 80 (2), 94–103.
URL http://dx.doi.org/10.1007/s00190-006-0036-x

Wieczorek, M., 2007. Gravity and topography of the terrestrial planets. Treatise on Geophysics 10, 165–206.

Wieczorek, M. A., Neumann, G. A., Nimmo, F., Kiefer, W. S., Taylor, G. J., Melosh, H. J., Phillips, R. J., Solomon, S. C., Andrews-Hanna, J. C., Asmar, S. W., Konopliv, A. S., Lemoine, F. G., Smith, D. E., Watkins, M. M., Williams, J. G., Zuber, M. T., Feb. 2013. The Crust of the Moon as Seen by GRAIL. Science 339, 671–675.

Wieczorek, M. A., Phillips, R. J., Jan. 1998. Potential anomalies on a sphere - Applications to the thickness of the lunar crust. Journal of Geophysical Research103, 1715.

Zuber, M. T., Smith, D. E., Lehman, D. H., Hoffman, T. L., Asmar, S. W., Watkins, M. M., Sep. 2013a. Gravity Recovery and Interior Laboratory (GRAIL): Mapping the Lunar Interior from Crust to Core. Space Science Reviews178, 3–24.

Zuber, M. T., Smith, D. E., Watkins, M. M., Asmar, S. W., Konopliv, A. S., Lemoine, F. G., Melosh, H. J., Neumann, G. A., Phillips, R. J., Solomon, S. C., Wieczorek, M. A., Williams, J. G., Goossens, S. J., Kruizinga, G., Mazarico, E., Park, R. S., Yuan, D.-N., Feb. 2013b. Gravity Field of the Moon from the Gravity Recovery and Interior Laboratory (GRAIL) Mission. Science 339, 668–671.